ČESKÉ VYSOKÉ UČENÍ TECHNICKÉ V PRAZE
Fakulta jaderná a fyzikálně inženýrská

VÝZKUMNÝ ÚKOL

2013

Karol Ješko

ČESKÉ VYSOKÉ UČENÍ TECHNICKÉ V PRAZE
Fakulta jaderná a fyzikálně inženýrská
Katedra fyziky

VÝZKUMNNÝ ÚKOL

Model elektronové rozdělovací funkce rýchlosti elektronů v blízkosti divertorových desek tokamaku JET

Electron velocity distribution function of JET divertor plasmas

Posluchač:	Karol Ješko
Školitel:	Ing. Ivan Ďuran, Ph.D.
Akademický rok:	2012/2013

ČESKÉ VYSOKÉ UČENÍ TECHNICKÉ V PRAZE
FAKULTA JADERNÁ A FYZIKÁLNĚ INŽENÝRSKÁ
PRAHA 1 - STARÉ MĚSTO, BŘEHOVÁ 7 - PSČ 115 19

Katedra: fyziky ***Akademický rok:*** 2012/13

VÝZKUMNÝ ÚKOL

Posluchač: Bc. Karol Ješko

Obor/Zaměření: Fyzika a technika termojaderné fúze

Vedoucí úkolu: Ing. Ivan Ďuran, Ph.D., Ústav fyziky plazmatu, AV ČR, v.v.i.

Konzultant: Mgr. Jan Horáček, Ph.D., Ústav fyziky plazmatu, AV ČR, v.v.i.

***Název úkolu (česky/anglicky)**:*
Model rozdělovací funkce rychlostí elektronů plazmatu v blízkosti divertorových desek tokamaku JET. / Model of electron velocity distribution function of JET divertor target plasmas.

***Pokyny pro vypracování**:*
Analyzujte možnosti další optimalizace, případně rozšíření, existujícího kódu pro výpočet rozdělovací funkce rychlostí elektronů plazmatu v blízkosti divertorových desek tokamaku JET. Zejména zvažte, popřípadě implementujte :

- adaptivní prostorové rozlišení podél magnetické siločáry v závislosti na lokální hodnotě střední volné dráhy,
- opuštění předpokladu maxwelovského rozdělení elektronů plazmatu podél mag. siločáry.

Proveďte první srovnání výsledků modelu s experimentálními daty měřenými pomocí systému Langmuirových sond instalovaných v deskách divertoru tokamaku JET.

Součástí zadání výzkumného úkolu je jeho uložení na webové stránky katedry.

Literatura:

1. F. F. Chen: Úvod do fyziky plazmatu, Academia, Praha, 1984
2. J. Wesson: Tokamaks, Clarendon Press – Oxford University press, 2004
3. P.C. Stangeby: The plasma boundary of magnetic fusion devices, IoP, 2000
4. I. H. Hutchinson: Principles of plasma diagnostic, Cambridge University press, 2002
5. J. Horáček et al.: Predicted effects of parallel temperature gradients on the overestimation of TCV divertor target Langmuir probe Te measurements, Journal of Nuclear Materials 313-316 (2003) 931-935.
6. M. Hron: Turbulence plazmatu na tokamaku CASTOR, disertační práce, MFF UK v Praze, 2002.

Datum zadání: 12.10.2012

Datum odevzdání: 30.06.2013

....
Vedoucí katedry

Čestné prohlášení

Prohlašuji na tomto místě, že jsem předloženou práci vypracoval samostatně a že jsem uvedl veškerou použitou literaturu.

Nemám závažný důvod proti užití tohto školního díla ve smyslu §60 Zákona č. 121/2000 Sb., o právu autorském, o právech souvisejících s právem autorským a o změně něktrerých zákonů (autorský zákon).

V Praze dne 11. září 2013

. . . .

Karol Ješko

Poďakovanie

Ďakujem Ing. Ivanovi Ďuranovi, Ph.D. za trpezlivé vedenie výskumnej úlohy a za mnoho užitočných rád a návrhov, ktoré ju obohatili.

Karol Ješko

Název práce: **Model elektronové rozdělovací funkce rýchlosti elektronů v blízkosti divertorových desek tokamaku JET**

Autor: Karol Ješko

Obor: Fyzika a technika termojaderné fúze

Druh práce: Výzkumný úkol

Vedoucí práce: Ing. Ivan Ďuran, Ph.D., Ústav fyziky plazmatu AV ČR, v. v. i.

Konzultant: Mgr. Jan Horáček, dr. és sc., Ústav fyziky plazmatu AV ČR, v. v. i.

Abstrakt: Táto práca priamo nadväzuje na a rozširuje moju bakalársku prácu [5]. V úvodných kapitolách obsahuje základný popis tokamaku JET a Langmuirovych sond. Hlavná časť práce spočíva v ďalšom vývoji modelu, ktorého úloha je určiť vplyv rýchlych elektrónov zo scrape-off layer na divertorové Langmuirove sondy a objasniť tým notorický problém nadhodnocovania elektrónovej teploty sondami pri vysokých hustotách v Scrape-off layer. Model konštruuje elektrónovú rozdeľovaciu funkciu rýchlosti elektrónov pri divertore z ktorej sa určí voltampérová charakteristika divertorovej Langmuirovej sondy a tým pádom aj elektrónová teplota. V tejto práci sú prezentované doterajšie výsledky simulácií pre tokamak TCV a JET. Pre tokamak JET je v závere práce prvé porovnanie výsledkov simulácií so skutočnými meraniami divertorových sond na JETe.

Klíčová slova: JET, Scrape-off layer, Divertor, Langmuirova sonda, Elektrónová teplota

Title: **Electron velocity distribution function of JET divertor plasmas**

Author: Karol Ješko

Abstract: This thesis follows and expands my bachelors thesis [5]. In the beginning, a basic description of the JET tokamak and Langmuir probes is given. The principal part of the thesis is about the further development of a simple model which aims at estimating the effect of suprathermal electrons originating in the SOL on divertor Langmuir probes and thereby clarify the problem of probe T_e overestimation for high densities in the SOL. The model calculates the electron velocity distribution function (EVDF) at the divertor. Using the EVDF, the probe IV characteristic and T_e can be calculated. In this thesis, results of simulations for tokamaks TCV and JET are presented. In the case of JET, a preliminary comparison of simulation results with experimental divertor LP data is done.

Key words: JET, Scrape-off layer, Divertor, Langmuir probe, Electron temperature

Contents

Chapter 1

The Joint European Torus

A number of relatively succesfull early tokamaks like T-3[1], ST[2] and TFR[3] provided the encouragement to make a big step towards a reactor concept. Europe agreed to pursue this goal by setting up a large scale collaborative project, the Joint European Torus - JET.

1.1 Design

The step to JET was indeed a large one. This can be appreciated by comparing its size to the largest then existing tokamak, TFR, a tokamak with a plasma volume of 1 m^3. The volume of JET turned out to be more than 100 m^3 and it was possible to stand in its vacuum vessel. It was not clear how to reach thermonuclear conditions, since the confinement properties of the hotter plasmas assumed in a large tokamak were unknown. This can also be considered as part of the justification of the JET experiment.

Another crucial incertainty was the limit for the β parameter, the ratio of the total energy of the plasma to the energy of the magnetic field. At a certain value of β, the plasma is vulnerable to MHD instabilities thus these impose a limit on β. In other words, for a given strength of the magnetic field, the plasma energy, proportional to the product of the density and temperature, can only reach a critical value.

A further problem were disruptions. It was experimentally confirmed that by increasing the plasma density beyond a critical value the plasma suddenly collapses. The critical density is called the Greenwald density. Disruptions can be fatal for the tokamak vessel and components, i.e. coils, since by collapsing the plasma there are no more charge carriers present, thus the current disappears, causing great forces of inductive character. The same process happens when the current is increased beyond a high value. However, the thermonuclear reaction rate rises with increasing density and higher current is believed to give better confinement. Hence, the disruption issue is crucial.

Given all these uncertainties the main technical parameters and geometry of the new tokamak had to be chosen.

[1] T-3 resulted from the Soviet tokamak programme in the 1960s, with temperatures of 1000 eV achieved.

[2] ST-Stellarator tokamak, located at Princeton Plasma Physics Laboratory, was originally a stellarator later converted into a tokamak. Here, high achievable temperatures were confirmed, however a new MHD instability, the sawtooth instability, was recognized.

[3] TFR-Tokamak de Fontenay aux Roses, located in a suburb of Paris, started operation in 1973. Temperatures of 2-3 keV were achieved, solely in Ohmic regimes.

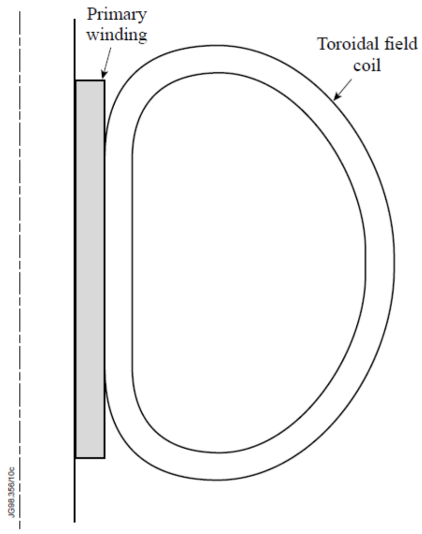

Figure 1.1: The D-shape of the JET toroidal field coils. [1]

1.1.1 Parameters and Geometry

The plasma current was chosen to be 3.8 MA, a value high enough the confine α-particles, with means to increase it to 4.8 MA. The toroidal field is limited by the force that the toroidal field coils can sustain. The toroidal magnetic field at the center of the plasma was chosen to be 2.8 T with the possibility of extending to 3.5 T.

Concerning the geometry of the plasma, practical matters were kept in mind [1]. The toroidal magnetic field falls as $1/R$, defining a high field side (HFS) and low field side (LFS). The well-known D-shape of the JET toroidal coils is chosen to minimize the force acting on the coils, which is greater at the high field side, HFS, fig. 1.1. At the HFS is supported by the central solenoid, whereas at the LFS the curvature of the coils helps to provide a balancing force to compensate the tensile stress.

The shape of the toroidal field coils define the shape of the vacuum chamber, giving a height-width ratio of 1.6. The aspect ratio was chosen to be 2.4. The main criterion for this choice was the minimization of costs [1].

The determination of the size of the plasma follows from the experimentally observed stability condition for the safety factor $q = 3$ approximately. Taking the geometric ratios from above and a toroidal field of 3 T, the requirement on q gives that the poloidal field B_p should not be greater than 0.5 T. The size of the plasma is then calculated from Ampere's law, which relates the poloidal field, total toroidal current and plasma minor radius. For a poloidal field of 0.5 T and a current of 4 MA, a minor radius a of at least 1 m is required. The major radius R and height b were conveniently rounded to 3 and 2 respectively, giving a minor radius of 1 m.

1.1.2 Heating

In the initial phase of a tokamak discharge, the plasma is Ohmically heated by the toroidal current. However, with increasing temperature the resistivity of the plasma falls. Therefore it can be stated that the Ohmic heating is self-limiting. For thermonuclear temperatures, Ohmic heating could not be counted on.

The heating of plasma by beams of neutral particles was already an established process at that time [1]. Ions of a chosen hydrogen isotope are produced which are then accelareted by a linear particle accelarator to the required energy. The particles are then neutralised in a cloud of neutral atoms by means of charge exchange. The beam still preserves its high energy and is injected into the tokamak plasma, penetrating until ionisation. The bean particles are then held by the magnetic field and transfer their energy to the plasma as they are slowed by collisions.

Another method of heating the tokamak plasma are high frequency electromagnetic waves generated by antennae inside the vacuum vessel. The antennae are placed in the limiter shade to prevent high heat fluxes and their melting. This technique is historically called Radio-Frequency (RF) heating. The rapidly oscillating electric field is set to a frequency which is in resonance with the cyclotron frequency of the plasma particles and this accelerates them to a higher energy. A number of heating schemes exist, and either the ions or electrons can be heated, depending on the heating scheme.

The magnitude of the heating was difficult to estimate provided the incertainty in the confinenement time. A possible goal for JET could be the achievement of breakeven, the regime when thermonuclear power equals the auxiliary heating power. This again is a problem, since the heating power required for breakeven conditions is inversely proportional to the square of the energy confinement time, $P_{\mathrm{H}} \sim 1/\tau_E^2$. It was pragmatically decided that the heating would be 3 MW with a possibility to increase it to 10 MW and 25 MW in stages.

1.1.3 Design proposal

The design team, led by Paul-Henri Rebut, started work on the design in September 1973 and the proposal was prepared by September 1975. The output of their work is document [2]. It has more than 600 pages and states the arguments for the specific JET design. It also provides a scan through tokamak physics then availabe and provides detailed design of many components for the future tokamak. Fig. **??** shows a cross section of basic elements of JET.

The Stated Aims

Along with the design, the aims were stated clearly in document [2]:

"The essential objective of JET is to obtain and study a plasma in conditions and dimensions approaching those needed in a thermonuclear reactor. These studies will be aimed at defining the parameters, the size and the working conditions of a tokamak reactor. The realisation of this objective involves four main areas of work:

1. the *scaling of plasma behaviour* as parameters approach the reactor range,
2. the *plasma-wall interaction* in these conditions,
3. the *study of plasma heating* and
4. the study of *α-particle production, confinement* and consequent *plasma heating.*"

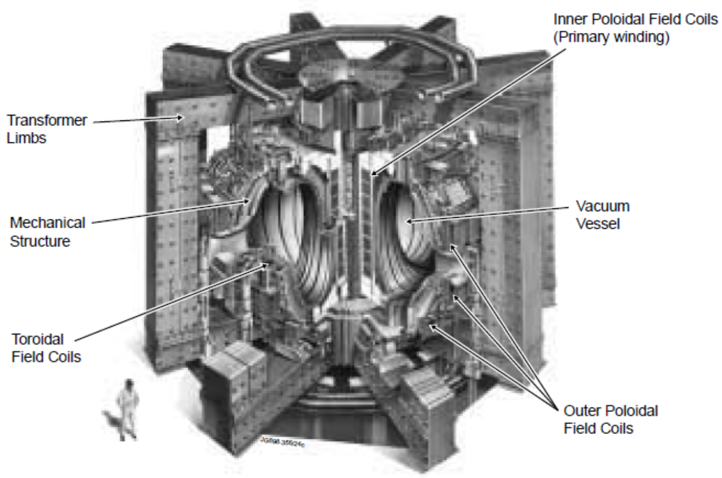

Figure 1.2: The basic components of JET, drawing. [1]

1.2 Construction

The JET facility needed a number of criteria to be fulfilled including the need to maintain and modify components from a remote location. This was due to activation of components due to neutron bombardment. Next, the components must have been assembled in a way that allowed necessary access. Fig. 1.3 shows the general layout.

1.2.1 Vacuum vessel

The main purpose of the vacuum vessel is to hold a vacuum with the pressure of the orders of 10^{-2} Pa. This would result that the force of the atmospheric pressure on 1 m^2 would be 10 tonnes [1]. Next, there was the need to clean the plasma-facing surface of the vessel from impurities by baking at temperatures 500 °C. Thus, this requires that the heating and cooling of the structure is not overloaded by stresses that are too large. A double skin was adapted for the vessel, through wich hot gas would pass to heat it.

The thickness of the material needed to sustain the stresses mentioned above would imply low electric resistance of the structure. Consequently, current driving field would also induce a large current in the vessel itself. This matter was solved by alternating the strong metal section of the vessel with sections with high resistance. The nickel alloy construction of the vessel thus needed eight kilometres of vacuum tight welds to connect the sections.

1.2.2 Field coils

The toroidal field was to be created by 32 D-shaped coils enclosing the vacuum vessel [1], each weighing 12 tonnes, Fig. 1.4(a). The coils were to carry currents of hundres of miliseconds and water was to be used to cool them. The magnetic field would trigger a tensile force on each of the coils and the poloidal field would provoke an additional force by interacting with the current in the coils. The combination of these two forces is a twisting force and was to be compensated by an outer mechanical structure. The structure is illustrated in Fig.1.4(b).

Poloidal field coils are naturally horizontal circular coils. They are placed outside the

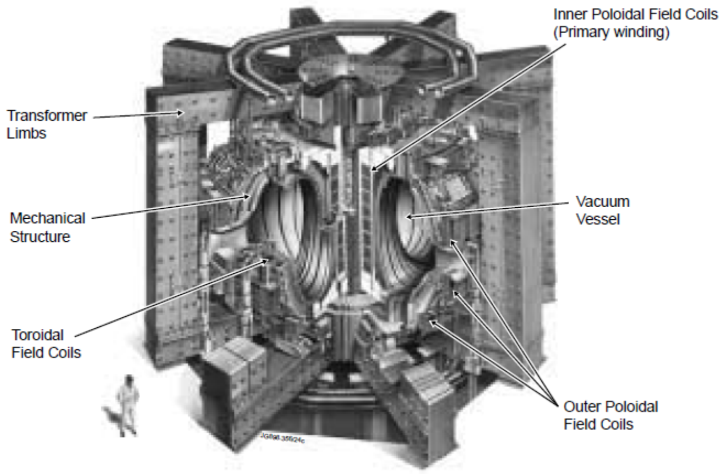

Figure 1.3: The basic components of JET, drawing. [1]

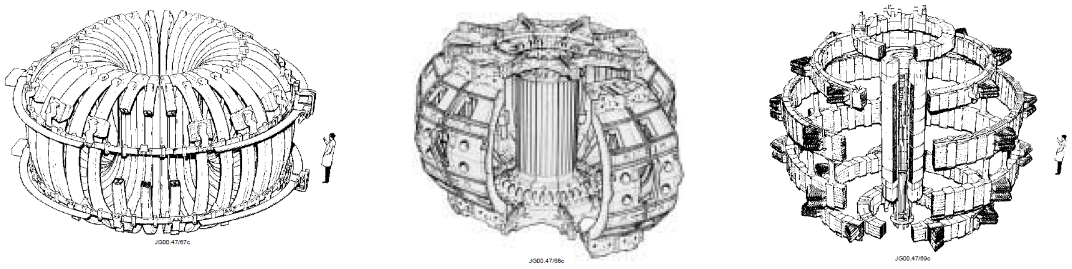

(a) (b) (c)

Figure 1.4: Layout of the toroidal field coils (a), support structure (b), poloidal field coils (c).

toroidal field coils and are illustrated in Fig. 1.4(c). The most important poloidal coil is the central solenoid which is wounded around the central column of an iron tranformer core, acting as a primary winding of the transformer. The other coils, six in total, are used to shape the plasma ring and control its position.

The tranformer core would envelope ale the components and with a weight of 2600 tonnes would dominate the appearance of JET.

1.2.3 Data acquisition and control

Each JET pulse would be accompanied by the creation of a large amount of data. Part of the data would be required for real time control of external systems. Another part of the data would be used to diagnose the plasma behaviour. Basic information from every shot is immediately sent to the control room. A broader scope of data would be stored and made available for post processing.

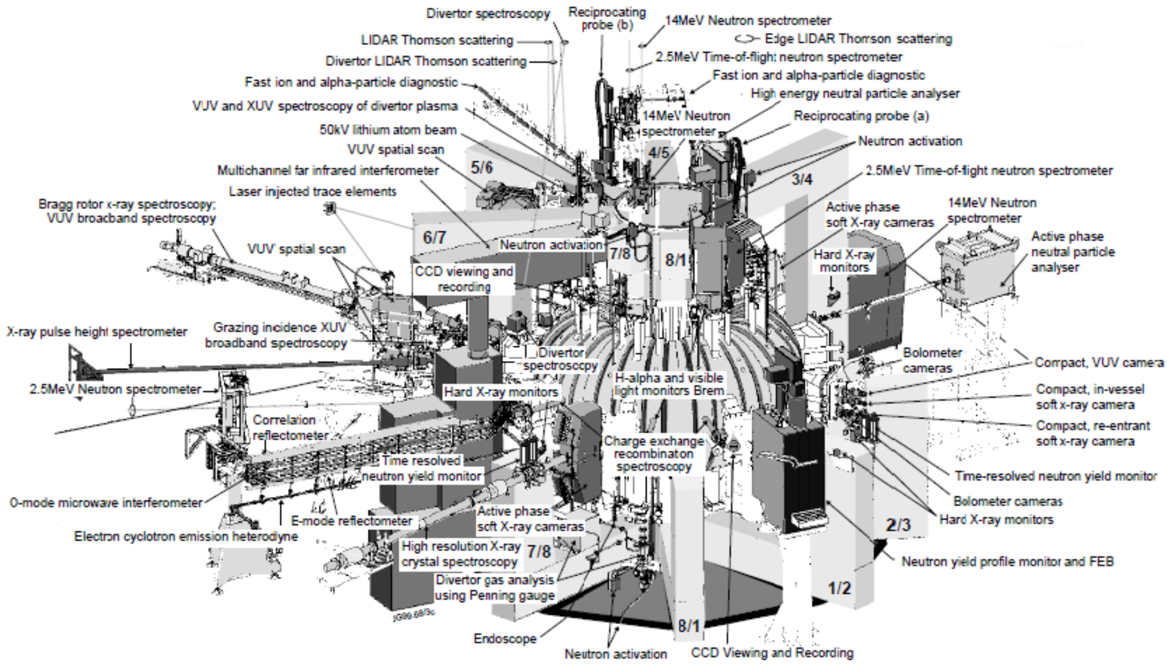

Figure 1.5: Layout of the JET diagnostic systems [1]

1.2.4 Diagnostics

The diagnostics installed at JET naturally required a much higher degree of sophistication than diagnostic systems on smaller devices. They had to be integrated into the the complex JET structure and not be vulnerable to radiation induced damage. The JET diagnostics would include:

- Small coils placed around the plasma detecting fluctutions in the magnetic field.
- Toroidal loops used to measure the voltage encircling the plasma.
- Electron cyclotron emission to estimate the temperature.
- Total radiated power estimated from the temperature drop by a set of bolometers.
- Neutron detectors measuring the D-D and D-T reaction rate.
- Ion temperature measurements by the injection of neutral particles.
- High resolution soft X-ray detectors.
- Robust interferometric measurements of the plasma density.
- Thomson scattering for measurement of the local density.
- Arrays of fixed Langmuir probes and reciprocationg probes.

The list above is by far not complete and lists only the basic diagnostics. The layout of the diagnostic system are illustrated in Fig. 1.5.

Chapter 2

Langmuir probes

2.1 Overview

Langmuir probes are inexpensive and relatively simple devices. They can be inserted into limiters or divertor targets in large arrays or into reciprocating drive mechanisms for probing deeper in the SOL [12]. In the first case, the probes are non-disturbing for the edge plasma. However, their interpretation is difficult and only a basic theory of operation will be given in this chapter.
The probe is virtually an electrically insulated conductive wire built into the limiter or divertor target plate. An electrically insulated metal object inserted into the plasma (thus electrically "floating") sits at floating potential V_{fl}, relative to the plasma sheath edge, where $V = 0$. Neglecting secondary electron emission, the floating potential has the form

$$V_{fl} = \frac{1}{2}\frac{kT_e}{e}\ln\left(2\pi\frac{m_e}{m_i}\left(1+\frac{T_i}{T_e}\right)\right) \tag{2.1}$$

In this case, the electron and ion flux densities are equal at the probe surface, $\Gamma_i = \Gamma_e$. Next, a probe that is not floating, but that is closed with the plasma via an external circuit will be considered. A potential difference can be applied via an external power supply, see Fig. 2.1. In this case, net current is drawn through the circuit, hence at the probe surface, $\Gamma_i \neq \Gamma_e$. The return surface is the divertor target surface or limiter surface.

By using charge conservation, the net current density to the Langmuir probe can be derived. A rigorous derivation can be found in [3]. The net current density j_{prb} to a probe biased to a potential V has the form

$$j_{prb} = en_{se}c_s\left(1-\exp\left(\frac{e(V-V_{fl})}{kT_e}\right)\right), \tag{2.2}$$

where n_{se} is the electron density at the sheath edge, c_s is the plasma sound speed and T_e the electron temperature at the probe.
When the probe is biased sufficiently negatively, all the electrons are repelled and all that remains is the ion current. This current is called the *ion saturation current* and is given by the equation

$$j_{sat}^{+} = en_{se}c_s. \tag{2.3}$$

Next, it will be shown that the analysis of the Langmuir probe circuit IV characteristic can yield measurements of the electron temperature T_e and density n_e at the probe. Let

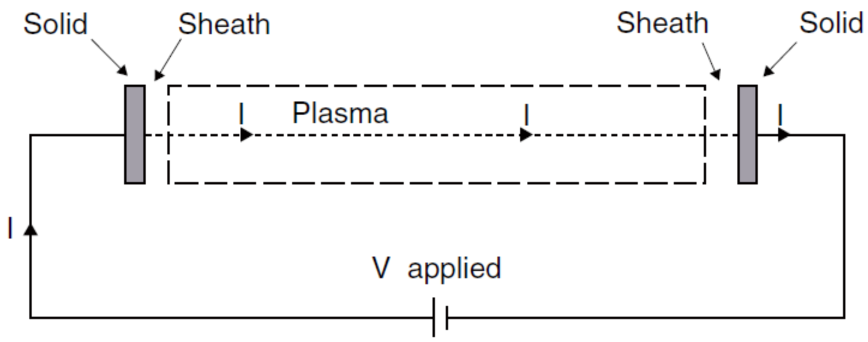

Figure 2.1: The probe circuit with an external power supply. One of the solid surfaces can be considered the probe surface and the other is the return surface. There is either no magnetic field, or **B** lies along the current direction [P. C. Stangeby, The plasma boundary of magnetic fusion devices]

A_{prb} be the area of the probe and let the magnetic field **B** be parallel to the normal vector of the probe surface. Then the total current passing through the probe is

$$I_{prb} = j_{prb} A_{prb}. \tag{2.4}$$

Combining equations 2.2, 2.3 and 2.4 gives the theoretical IV characteristic of the probe

$$V_{prb} = \frac{kT_e}{e} \ln\left(1 - \frac{I_{prb}}{I_{sat}^+}\right). \tag{2.5}$$

Consequently, a logarithmic fit of V_{prb} against I_{prb} yields a measurement of T_e. Since

$$I_{sat}^+ = A_{prb} e n_{se} c_s, \tag{2.6}$$

it can be seen that the fit also yields the electron density at the sheath edge, very close to the probe.

Equation 2.2 holds only for probe potential which are lower than the plasma potential. If the probe potential equals the plasma potential, no sheath electric field is present and electrons are not repelled by the sheath anymore, flowing to the probe at a thermal velocity distribution. This is called electron saturation, and the *electron saturation current* is given by

$$I_{sat}^- = -\frac{1}{4} ne\langle v_e\rangle, \tag{2.7}$$

where $\langle v_e\rangle$ is the electron thermal speed and n is the electron density just at the probe. Since electrons carry the same absolute charge but are much lighter, electron saturation current is greater than the ion saturation current by the ratio $(m_i/m_e)^{1/2} \approx 60$ for a hydrogen plasma. However, for values of V_{prb} causing electron saturation, currents drawn from the plasma are so large and disturbing that any simple analysis trying to solve the problem fails. The effect of electron saturation on Langmuir probe T_e measurements will be discussed in section 2.5.

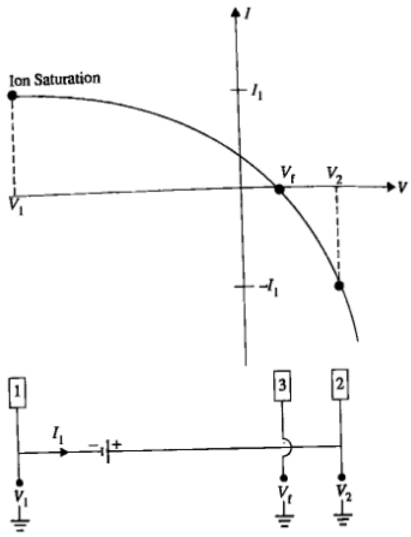

Figure 2.2: Schematic illustration of the triple Langmuir probe configuration. The circuit diagram shows the positions of the probes on the $I(V)$ curve [J. Wesson, Tokamaks]

2.2 Single probes

The probe described in section 2 is in fact the actual single Langmuir probe. The current drawn by the probe from the plasma is returned by either the limiter surface or divertor target plate. The main requirement for a return surface area is that it should be large enough so that a small potential change across the return surface sheath will enable the return current to flow. Hence, the surface carrying the return current must not reach the ion saturation limit before the probe reaches electron saturation. In a hydrogen plasma, the return surface should be larger than the probe area by the electron to ion saturation current ratio, which is typically ≈ 60, section 2.

2.3 Double probes

A double Langmuir probe is a pair of probe tips close enough to each other so that they are assumed to be exposed to the same plasma conditions. The probes are kept isolated from the torus and are connected across a variable biasing voltage source. Let the currents in each probe tip be I_1, I_2. Taking two identical probes with surface A, defining the power supply voltage $V = V_1 - V_2$, where V_1, V_2 are the respective probe voltages and defining the currents with equation 2.2 the following theoretical relation can be calculated

$$I_1 = I^+_{sat} \tanh \frac{V}{2T_e} \tag{2.8}$$

The main advantage of this configuration is that limits the electron current, thus preventing destruction of the probe.

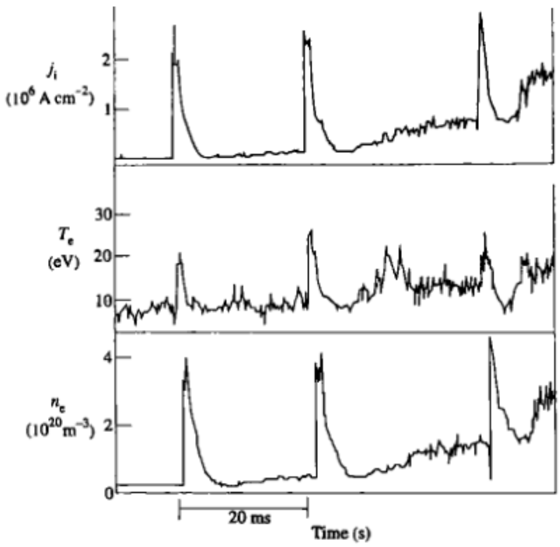

Figure 2.3: Divertor target triple probe measurements during an ELM discharge at JET [J. Wesson, Tokamaks]

2.4 Triple probes

Triple Langmuir probes consist of three tips exposed to the same plasma parameters. One of the probe tips measures the floating potential while the other two are coupled and biased with a constant potential so that one tip draws the ion saturation current and the other an electron current, see Fig. 2.2. The potential V_2 on the electron current drawing tip adjusts itself so that the two currents are of the same size. Let the tips be identical, of surface A. Again, using equation 2.2 and $I_1 + I_2 = 0$,

$$(1 - \exp\left(\frac{e(V_1 - V_{fl})}{kT_e}\right))A + (1 - \exp\left(\frac{e(V_2 - V_{fl})}{kT_e}\right))A = 0 \tag{2.9}$$

Assuming the supply voltage to be large, $kT_e \ll e|V_1 - V_{fl}|$, equation 2.9 gives the following expression for the temperature

$$T_e = \frac{(V_2 - V_f)}{k \ln 2} \tag{2.10}$$

Since in this case V_2, V_{fl} and I^+_{sat} can be measured at the same time, high time resolution is an advantage of this arrangement. Thanks to this triple probes are frequently used to measure ELM discharges. Fig. 2.3 shows high time resolution divertor triple probe measurments from JET. However, triple probe data are unreliable in situations when plasma parameters differ across the three probe tips or when I^+_{sat} and I^-_{sat} are comparable [?].

2.5 Langmuir probe disadvantages

The main disadvantage of Langmuir probes is that in order to measure spatial temperature or density profiles, they have to be inserted into the plasma, thus there can be a distortion of measurement due to the intrusion of the probe. So, the probe body should be small enough to minimize perturbation.

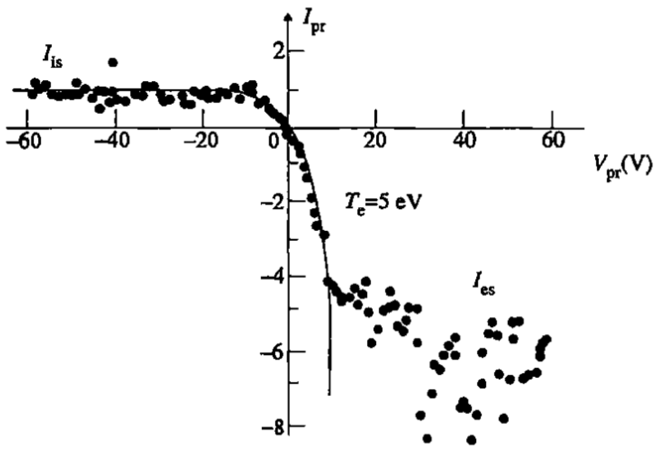

Figure 2.4: A single Langmuir probe characteristic from the T-10 tokamak [J. Wesson, Tokamaks]

Another disadvantage is the interpretation of Langmuir probe measurements, which can be quite a challenge, as reported in section 2. For non magnetized ($\mathbf{B} = \mathbf{0}$) plasmas it is found, in accord with section 2, that the electron to ion saturation current ratio is

$$\frac{j_{sat}^{-}}{j_{sat}^{+}} = \left(\frac{m_i}{m_e}\right)^{1/2}. \tag{2.11}$$

However, when $\mathbf{B} \neq \mathbf{0}$ far smaller ratios are usually recorded. It appears that equation 2.1 does not hold for voltages higher than the floating potential, see Fig. 2.4, an experimental IV characteristic from the T-10 tokamak. The data is fitted up to the point where the roll over into electron saturation occurs.The reason for this is not clear. It appears that resistances within the plasma itself have something to do with this problem [3]. So, commonly only the net-ion collecting path is used to obtain measurements of plasma parameters [12]. Unfortunately, this causes that only the tail of the electron distribution, comprising around 5% of the total is measured [?]. If the distribution is non-maxwellian, this can result into incorrect, more precisely too high values of T_e [3] being measured by the standard analysis of the probe IV characteristic. Identifying the causes of the non-maxwellity of the electron distribution and its treatment to achieve a correction to Langmuir probe T_e measurements are the main objectives of chapter 5.

Some comparisons with other measurement techniques are shown in Fig. 2.5 and Fig. 2.6. In both figures, it is clearly seen that Langmuir probe measurements yield higher electron temperatures than alternative methods, i. e. lithium beam injection[1] and Thomson scattering.

[1] A diagnostic method involving the Zeeman effect on a high-energy neutral lithium beam injected into the plasma. Both the electron density and temperature can be measured. A detailed analysis on neutral atom diagnostics can be found in [4].

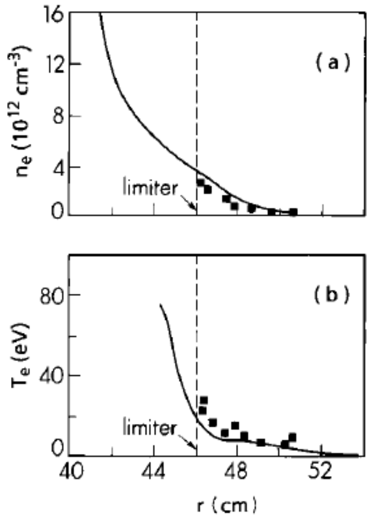

Figure 2.5: Measurements of n_e and T_e in the TEXTOR tokamak using a lithium beam (continuous line) and a Langmuir probe (points). [P. C. Stangeby, G. M. McCracken, Nuclear Fusion, Vol. 30, No. (1990) 1225]

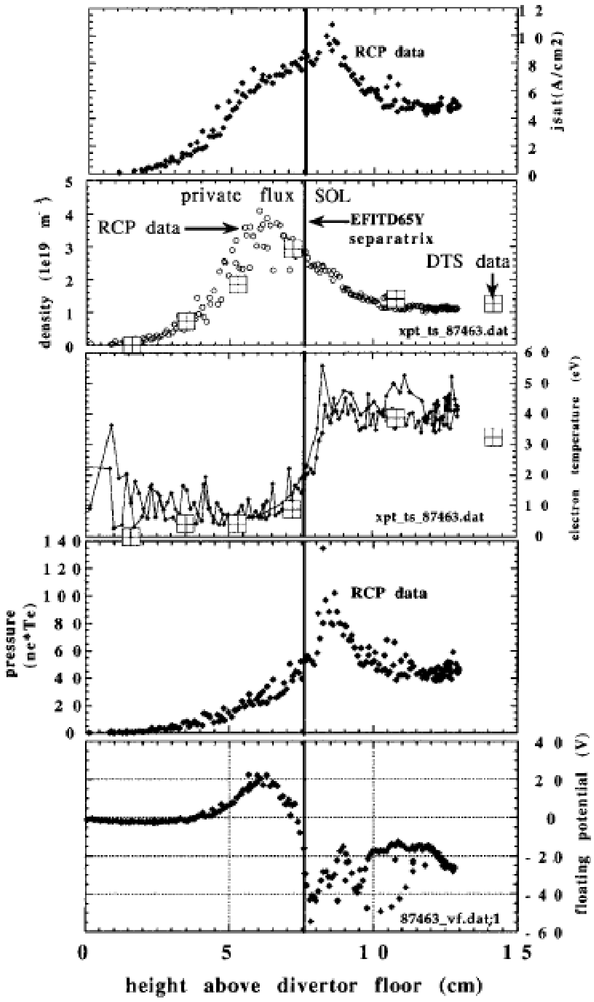

Figure 2.6: Vertical profiles of n_e and T_e above the divertor target floor in the DIII-D tokamak using Langmuir probes (RCP) and Thomson scattering (DTS). [J. G. Watkins, R. A. Moyer, J. W. Cubbertson et al., Journal of Nuclear Materials 241-243 (1997) 645]

Chapter 3

EVDF model description

3.1 Background

Langmuir probes are commonly used to measure plasma parameters, such as the electron temperature or plasma density in the plasma edge. It is an inexpensive and relatively simple method, however there is a variety of observations showing that under some specific conditions the electron temperature T_e measured by probes can significantly differ from the actual T_e in the SOL. For example, in [14] it is reported that during ohmic heating in the ASDEX tokamak the T_e measured by Langmuir probes is at least two times higher than the one measured by Thomson scattering. In [7] it is reported that in strongly recombining detached or partially detached divertor plasmas on TCV the expected $T_e \sim 1$ eV is not reproduced by probes. Instead, measured values of approximately $T_e \sim 5$ eV are typical.

Thus from section 2 this indicates that the electron velocity distribution function (EVDF) at the plasma edge deviates strongly from a Maxwellian distribution. A reason for this deviation can be fast electrons originating in further upstream of the divertor which may travel collisionlessly to the targets [7]. De-Maxwellization of the EVDF is also affected by a number of processes in the SOL like inelastic collisions of electrons with neutrals and impurities or fast-time processes like edge-localized modes (ELMs) and blobs [8]. In the next two sections, two possible approaches to treat this problem are introduced. The description and interpretation of the latter is one of the main aims of this thesis.

PIC simulations

In paper [8] a self-consistent, massively parallel PIC[1] simulation is used to calculate non-maxwellian EVDFs at divertor target triple probes at JET. The simulation is performed for stationary SOL conditions as well as for ELMs. The key player of the simulation is the ratio of elastic and inelastic collisions. In Fig. 3.1 calculated distribution functions for different collisionalities and SOL regimes are shown. Electron collisionality ν^* is defined as the ratio of electron-electron collision frequency and the electron bounce frequency. The bounce frequency is that at which electrons trapped on banana orbits oscillate. The paper concludes that for moderate divertor plasma collisionalities, triple Langmuir probes can overestimate the electron temperature by factor of five. On the contrary, for ELM discharges, probes underestimate peak values of T_e up to 70% [8].

[1] The Particle-in-Cell (PIC) method refers to a technique used to solve a certain class of partial differential equations. In this method, individual particles (or fluid elements) are tracked in continuous phase space,

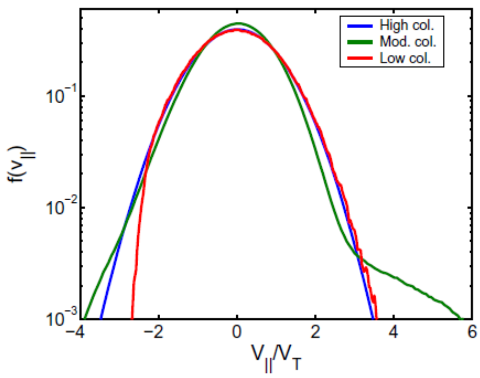

Figure 3.1: Normalized EVDFs at the position of a triple Langmuir probe for stationary SOL with different collisionalities. [D. Tskhakaya et al., Journal of Nuclear Materials 415 (2011) 860-864].

3.2 Simple kinetic model

Self-consistent simulations described in section 3.1 require powerful supercomputers[2] and significant amounts of time to perform the computation. Another approach to the problem is to try to identify and handle the main phenomenon responsible for the non-maxwellity of the EVDF, thus requiring much lower computational power. One of the aims of this thesis is the detailed description and interpretation of the results of such a model, namely the model described in the paper of J. Horáček et al. [7]. The phenomenon behind the de-maxwellization of the EVDF is believed to be the presence of large parallel temperature gradients in the SOL. The parallel T_e gradients lead to the enhancement of the tail of the EVDF and, from section 2, probes evaluate the temperature primarily from the tail of the EVDF, hence leading to T_e overestimation. The simulations are carried out for TCV and JET input data.

The idea of the model is the numerical construction of EVDFs at the divertor target, where the electron temperature T_e is measured by Langmuir probes. From the EVDF, Langmuir probe IV characteristics, section 2, can be derived.

3.3 Input data

As an input, the model requires parallel $T_e(x)$ and $n_e(x)$ SOL profiles, where x is the connection distance, starting from position $x = 0$, the inner divertor target plate and ending at $x = L$, the outer divertor target plate. The model also includes potential variation. The potential profile $\phi(x)$ can readily be calculated from the temperature profile, according to [9], as $\phi(x) = 0.71k(T(x) - T(0))$ As stated in section 3.2, the simulation is carried out for TCV and JET input data.

whereas moments of the distribution such as densities and currents are computed simultaneously.

[2] All simulations from the paper of D. Tskhakaya et al. [8] have been performed on HECTOR (Edinburgh, UK) and HPC-FF (Jülich, Germany) supercomputers. Times required for a single simulation on 512 processors ranged from 24 to 36 hours.

TCV

Experimental data of parallel $T_e(x)$ and $n_e(x)$ are unavailable, thus profiles obtained from fluid simulations were used, in particular, profiles generated by the B2-EIRENE[3] code. The parallel electron temperature and density are the results of any converged solution. The simulation uses results computed by the SOLPS4 B2-EIRENE package with no drifts included and with carbon as the only impurity species [7]. In Fig. 3.2, the parallel T_e and n_e profiles are plotted against the x-coordinate, i.e. the position along the magnetic field line. The profiles are situated in the flux surface at distance 1.8 mm outside the midplane separatrix. Low density cases may be regarded as low recycling solutions, while higher density corresponds to high recycling conditions [7].

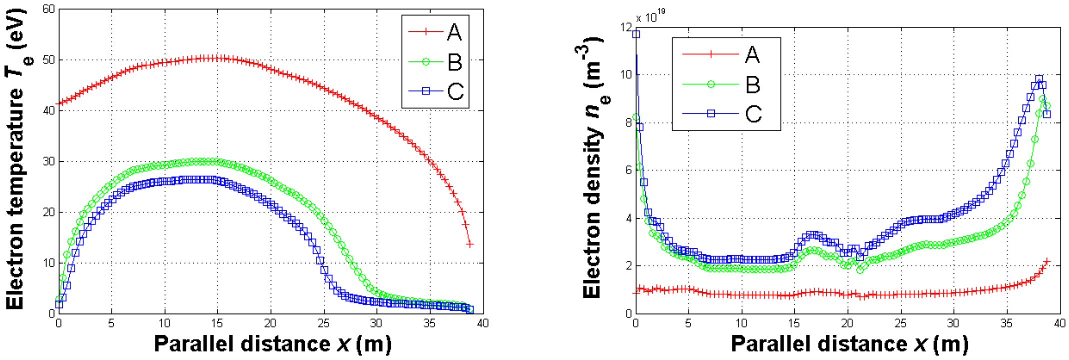

(a) (b)

Figure 3.2: Computed parallel T_e (a) and n_e (b) profiles from the B2-EIRENE code, for the flux surface situated 1.8 mm from the separatrix. The labels A, B, C denote increasing midplane density, $n_e^m = 8$, 23 and 33 $.10^{-18}$ m^{-3} respectively. The x-coordinate spans from the inner divertor target to the outer divertor target.

JET

As experimental data are not available, parallel profiles of T_e and n_e computed by the two-dimensional multifluid EDGE-2D code coupled to the Monte Carlo EIRENE impurity code were used [6]. This code package was used to model shots from JET Ex-3.1.2[4], corresponing to JPNs 81469-81480. One of the many outputs of the EDGE2D/EIRENE code are the parallel T_e and n_e profiles. As the independent variable for the profiles, the midplane separatrix density is used for reasons explained below. In Fig. 3.3, three EDGE2D/EIRENE computed T_e and n_e profiles are visible, each corresponding to a different midplane separatrix density case. Each case, its corresponding density and its label are shown in Tab. tab:densities.

Each of these profiles is part of the solution of one entire converged EDGE2D/EIRENE run for a given set of (experimentally measured) input parameters. Hence the obtained profiles can be regarded as the actual profiles at the time when the input parameters were

[3]B2-EIRENE is a two-dimensional plasma edge fluid code. The code package was developed for TEXTOR applications in the late 1980s. It has become a standard tool in plasma edge science. Currently it is mainly used for divertor configurations, also by the ITER central team in order to assist in designing the ITER divertor, see [17]

[4]The objective of this experiment was to perform a low-δ L-mode density scan at fixed input power in order to characterize detached plasmas.

Density case	Label	Midplane separatrix density
Low	E	0.50×10^{19} m^{-3}
Intermediate	F	1.20×10^{19} m^{-3}
High	G	1.75×10^{19} m^{-3}

Table 3.1: Values of midpalne separatrix densities corresponding to parallel T_e and n_e profiles E, F, G in Fig. 3.3, from EDGE2D

.

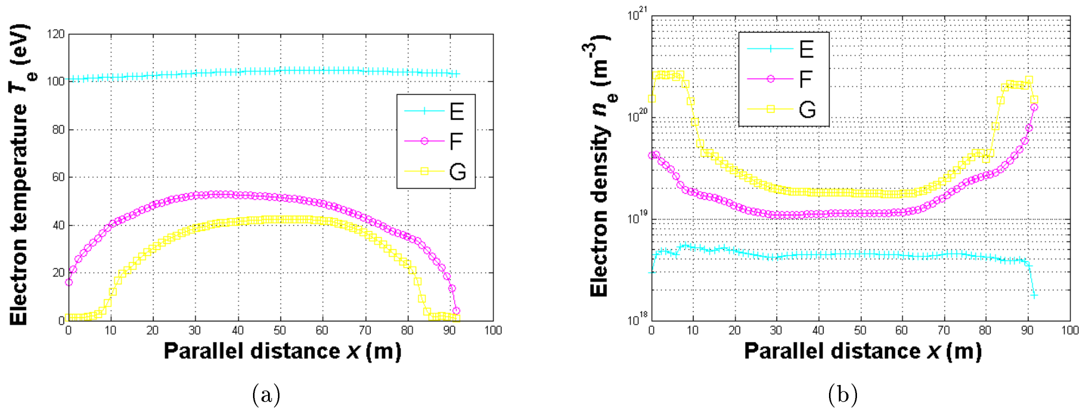

Figure 3.3: Computed parallel T_e (a) and n_e (b) profiles for the JET tokamak. The labels E, F, G denote increasing midplane density (E being a low, F intermediate and G a high density case). The x-coordinate spans from the inner divertor target to the outer divertor target. For better visibility, the n_e profile is plotted logarithmically.

measured. Let us examine JPN 81469, a density ramp up discharge ending with a disruption. The temporal evolution of line averaged density for this pulse, from interferometric measurements, can be seen in Fig. 3.4. For each timeslice, we can get the actual parallel profiles in the SOL by matching the separatrix density of the simulated profile to the experimental separatrix density, measured by HRTS. We use data from such EDGE2D runs to describe divertor conditions with respect to midplane separatrix density. In Fig. 3.5 divertor densities from EDGE2D as a function of the midplane separatrix density can be seen.

3.4 EVDF construction

Fast electrons from the warmer upstream regions can travel collisionlessly to the targets, thus affecting the distribution function. The contribution of these electrons to the target EVDF is constructed numerically. The $T(x), n(x), \phi(x)$ profiles are specified. The principle of the model:

1. First, a specific value of v_0 is chosen at the target. The x-coordinate at the target is, naturally, $x = 0$.

2. Next, the mean free path $\lambda(0)$ of the electron with velocity v_0 in the target plasma characterised by $T_e(0)$ and $n_e(0)$ is calculated. The choice of the formula for the mean free path will be discussed in section 3.6.

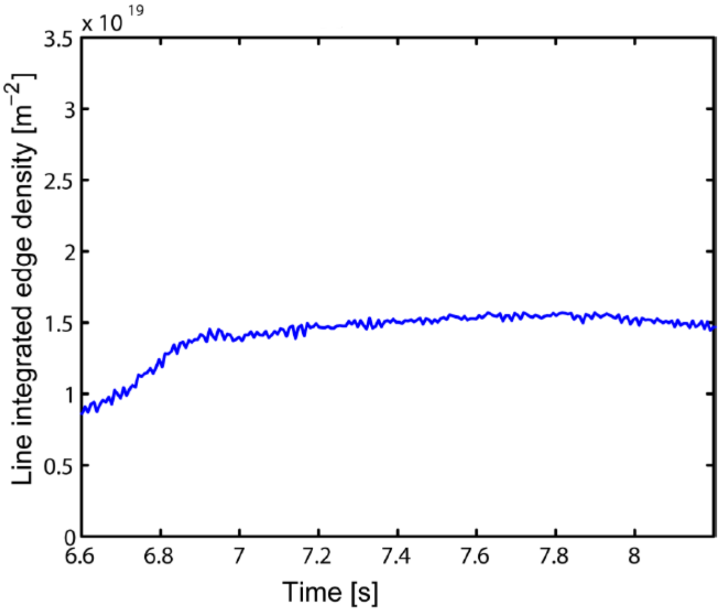

Figure 3.4: Interferometric measurement of line integrated density from the KG1V/LID4 diagnostic, JPN 81469. A typical density ramp discharge, used as a benchmark for EDGE2D/EIRENE modelling.

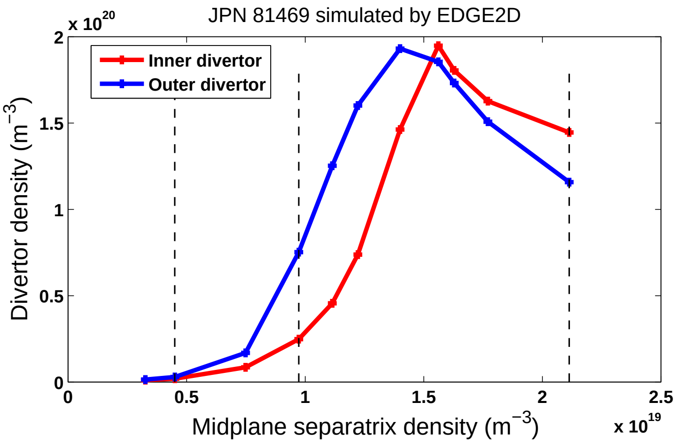

Figure 3.5: Divertor densities as a function of the midplane separatrix density from the EDGE2D code, simulating JPN 81469.

3. Now, a small step, typically a small fraction of the local mean free path $\mathrm{d}x$ upstream is taken [5]. The x-coordinate of the electron is now $x = 0 + \mathrm{d}x$.

4. Subsequently, the probabilty of a collision occuring during this step is calculated classicaly, $\mathrm{d}p = \frac{\mathrm{d}x}{\lambda}$.

5. During the step, in consequence of the potential change, the velocity changes too. The

[5] The results in [5] used a constant step dx for both TCV and JET input data. In this work the JET case has been recalculated by the new version of the code with the step as a fraction of the local MFP, while the less important TCV case was not.

new velocity is found, from energy conservation: $v(x) = \sqrt{v_0^2 + \frac{2e}{m_e}(\phi(x) - \phi(0))}$.

6. Again, the mean free path $\lambda(v, x)$ is calculated for $T_e(x), n_e(x)$, v and the probabilty of collision during the next step $\mathrm{d}p(x)$ is computed.

7. The procedure described above is repeated. As the electron advances further upstream, the total probablity of collision accumulates. The accumulated probability of collision at point x_u upstream is the sum of the probabilities of collision during each step and can be written as

$$p(x_u, v_0) = \int_0^{x_u} \mathrm{d}p(x) = \int_0^{x_u} \frac{\mathrm{d}x}{\lambda(v_0, x)} = \int_0^{x_u} \frac{\mathrm{d}x}{\lambda(v(\phi(x), v_0), T_e(x), n_e(x))}. \quad (3.1)$$

8. Naturally, the process is repeated until a point with coordinate x^* is reached, where the accumulated probability of collision reaches unity, i. e. where $p(x^*, v_0) = 1$.

9. It is assumed that a Maxwellian EVDF exists $f^{\mathrm{Max}}(v)$ at every point x along the field line. Since an electron with "terminal" velocity v_0 at the target could have traveled collisionlessly from points $x < x^*$, the target electron velocity distribution function can then be evaluated as the "average" EVDF along to field line from $x = 0$ until the point $x = x^*$ [9]:

$$f(v_0) = \frac{1}{x^*} \int_0^{x^*} S(x) f^{\mathrm{Max}}(T_e(x), n_e(x), v(x, v_0)) \mathrm{d}x, \quad (3.2)$$

where the weighting function $S(x) = \exp(-p(x))$ represents a suitable electron source distribution [7]. The physical meaning of this weighting function is that electrons originating closer to the target have a greater chance of reaching the target than from sources further upstream, thus EVDFs closer to the target count more in integral 3.2.

10. By repeating this process for a range of values of v_0, the entire EVDF at the target is constructed.

3.5 IV characteristic construction

Now that the synthetic EVDF simulating the "real" EVDF at the target is known, the divertor target probe IV characteristic can be constructed. This is done by calculating the *cutoff velocity* v_{cutoff}, the minimum velocity at which electrons can overcome the sheath potential of an electrically floating probe, section 2. At the probe(again under floating conditions), the ambipolar condition must be satisfied, i.e. the electron and ion currents must be equal,

$$j^-_{prb} = j^+_{prb}. \quad (3.3)$$

The ions enter the sheath at the sound speed, hence

$$j^+_{prb} = en_{se}c_s, \quad (3.4)$$

where n_{se} is the density at the sheath edge and c_s the ion sound speed. The ion and electron temperatures and densities are assumed to be equal, $T_i = T_e, n_i = n_e$, therefore $n_{se} = n_e(0)$ and $c_s = \sqrt{\frac{2kT_e(0)}{m_i}}$. Since the EVDF at the target is known, the electron current to the probe can readily be calculated as

$$j^-_{prb} = e \int_{v_{\text{cutoff}}}^{\infty} v_0 f(v_0) \mathrm{d}v_0. \tag{3.5}$$

Thus by substituting 3.4 and 3.5 into the ambipolar condition 3.3 the following equation is obtained

$$\int_{v_{\text{cutoff}}}^{\infty} v_0 f(v_0) \mathrm{d}v_0 = \sqrt{\frac{2kT_e(0)}{m_i}}. \tag{3.6}$$

The only unknown parameter in this equation is the cutoff velocity v_{cutoff} and so it can be determined from this equation. Once this has been done, the actual IV characteristic can be constructed. So far, the calculations dealt with an electrically isolated i. e. floating probe. Now, a potential V_{prb} shall be applied to the probe. This potential defines a new velocity w at which electrons can overcome the sheath. Since a floating probe is biased negatively, an applied potential will decrease the velocity necessary to overcome the total potential, thus giving w as

$$w = \sqrt{\frac{2}{m_e}\left(\frac{1}{2} m_e v_{\text{cutoff}}^2 - eV_{prb}\right)}. \tag{3.7}$$

The new electron current to the probe is given by

$$j^-_{prb}(V_{prb}) = e \int_{w}^{\infty} v_0 f(v_0) \mathrm{d}v_0. \tag{3.8}$$

The ion current remains unchanged and so net current is now drawn through the probe. This current is easily given by subtracting the electron current from the ion current,

$$j_{prb}(V_{prb}) = j^+_{prb} - j^-_{prb}(V_{prb}). \tag{3.9}$$

Finally, expression 3.9 is the actual IV characterstic of the target probe.

3.6 Choice of mean free path

In this section, the formula used to calculate the mean free path will be introduced. Following Stangeby's draft [9], expressions from the NRL Plasma formulary are used [15]. Let the index α refer to test electrons with velocity v_α and index β to the actual plasma particles into which the test particles are injected, with temperature $T_e(x)$ and density $n_e(x)$. Let $\chi^{\alpha/\beta} = \frac{m_\beta v_\alpha^2}{2kT_\alpha}$. [15] gives the various collision frequencies for fast electrons, that is to say when $\chi \gg 1$.

For stopping:

$$\nu_s = 7.7 \times 10^{-6} n \ln(\Lambda) \epsilon^{-3/2} \tag{3.10}$$

For perpendicular diffusion:

$$\nu_\perp = 7.7 \times 10^{-6} n \ln(\Lambda) \epsilon^{-3/2} \tag{3.11}$$

For parallel diffusion:

$$\nu_\| = 3.9 \times 10^{-6} n \ln(\Lambda) T \epsilon^{-5/2} \tag{3.12}$$

For energy:

$$\nu_\epsilon = 2\nu_s - \nu_\perp - \nu_\| \tag{3.13}$$

Where $\epsilon = \frac{1}{2e} m_e v^2$. In equations 3.10-3.13, $\nu[\mathrm{s}^{-1}], n[\mathrm{cm}^{-3}], T, \epsilon[\mathrm{eV}]$. According to [3], $\ln \Lambda = 17$ shall be used. From equations 3.10-3.13 the electron-electron collision mean free path can be expressed

$$\lambda_{\text{fast}}(\epsilon, T, n) = \frac{v_\epsilon}{\nu} = \frac{10^{12} \epsilon^2 \sqrt{\frac{2e}{m_e}}}{n \ln \Lambda (7,7 - 3,9 \frac{T_e}{\epsilon})} \tag{3.14}$$

For thermal electrons, $\epsilon = T$ and $\chi^{\alpha/\beta} = 1$, the thermal mean free path is used

$$\lambda_{\text{thermal}}(T, n) = 0,92 \times 10^{16} \frac{T^2}{n} \tag{3.15}$$

It is necessary to connect these two expressions in some way, so that the resulting mean free path is a continuos function of v. We have decided to use the following expression to calculate the mean free path:

$$\lambda(\epsilon, T, n) = \lambda_{\text{fast}} - (\lambda_{\text{fast}} - \lambda_{\text{thermal}}) \exp\big(-(1 - \frac{\epsilon}{2T_e})^2\big). \tag{3.16}$$

This expression provides smooth transition from the thermal mean free path to the super-thermal mean free path, Fig. 3.6. Electrons are regarded as thermal until two times the local T_e. Throughout the model, expression 3.15 is used for thermal and expression 3.16 for super-thermal electrons. However, it is not guaranteed that this approach is correct. Further, these formulae are computed only for a Maxwellian non-magnetized plasma. Future activity may include research on electron mean free paths in a magnetized plasma.

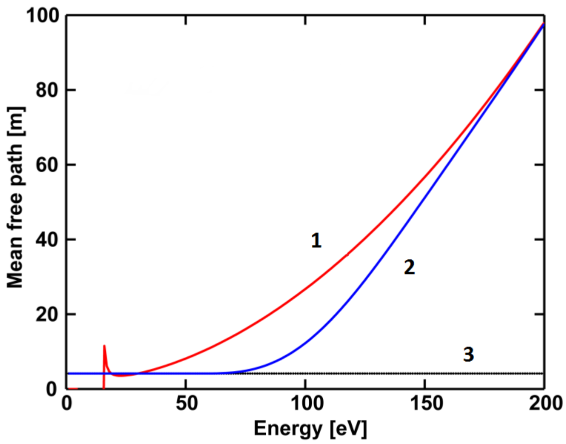

Figure 3.6: Mean free paths λ_{fast} (1), $\lambda_{\mathrm{thermal}}$ (3) and λ (2) of an electron with energy ϵ in a plasma at fixed temperature $T_e = 30$ eV and density $n_e = 2 \times 10^{19}\mathrm{m}^{-3}$.

Chapter 4

Results

In this section, results obtained from the simulation decribed in sections 3.4, 3.5 and 3.6 will be presented and interpreted for both TCV and JET input data. For TCV data, accord with the results in paper [7] will be shown. For JET, a comparison of experimental data with the model is made.

4.1 Results for TCV

4.1.1 Basic interpretation

It is expected that the electron velocity distribution function at the divertor target will be distorted, i. e. that the "tail" of the EVDF will be somewhat higher. Indeed, the model yields such EVDFs. The effect is most visible when a significant temperature gradient is present. This condition is met for the B profile, for example, section **??** and the corresponding EVDF is shown in Fig. 4.1. Similar more or less significant distortions can be observed for the rest of the profiles as well, depending on the temperature gradient. However, we are more interested in the IV characteristics, since the temperature is obtained from them. The IV characteristic is calculated from the distribution function as described in section 3.5 in a range of voltages pertinent to a real situation, from -100 V to 50 V. Next, the computed characteristic is fitted by equation 2.5 in order to obtain the electron temperature, just like as if it was experimental data. Assuming our model is correct, this is the temperature that a probe inserted in the given plasma is supposed to measure.

In Fig. 4.2 two examples of IV characteristics for the inner divertor target for profiles A (less significant temperature gradient) and B (significant temperature gradient) are shown. In the case of the less significant temperature gradient, the computed EVDF and the corresponding IV characteristic the temperature T_e predicted by the model lies between the target T_0e and maximum upstream temperature T_u, Fig. 4.2(a). For the high temperature gradient in profile B, the computed EVDF and IV characteristic are more distorted and the computation yields T_e that is by a factor of ~ 2 higher than the target temperature predicted by the B2-EIRENE code, Fig. 4.2(b).

4.1.2 Density scan for TCV

Fig. 4.3 compiles the main results of the model. By fitting the computed IV characteristics for each profile of the selected flux surface (a total of 8 parallel profiles) the temperatures (simulating Langmuir probe measurements) are obtained. These are plotted with respect

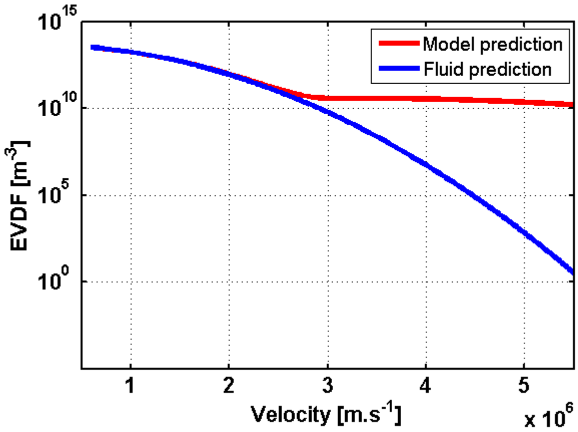

Figure 4.1: Distorted EVDF computed by the model (red) and Maxwellian EVDF (blue) at the inner divertor target. The distorted EVDF is calculated for profile B and the Maxwellian at the target is calculated for $T_e(0)$ and $n_e(0)$ from the B2-EIRENE fluid code. The y-axis uses logarithmic scaling due to poor visibility when using normal scaling.

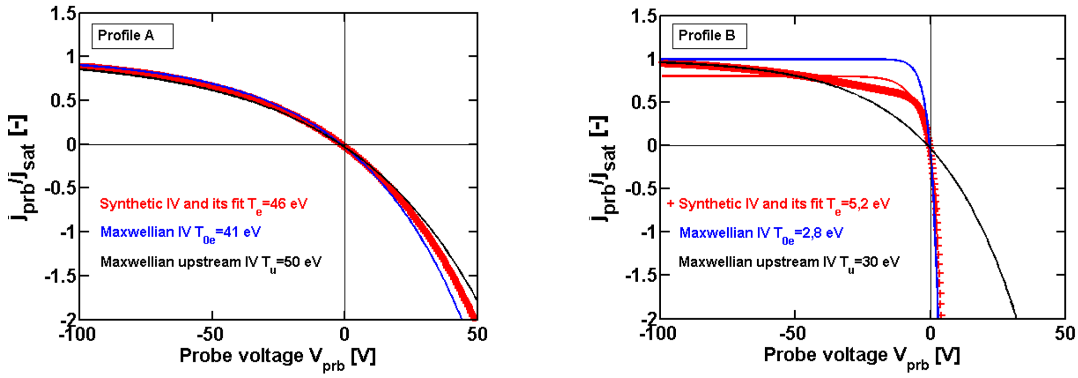

(a) (b)

Figure 4.2: Computed IV characteristics at the target (red+) and their fits (red) compared to IV characteristics obtained for T_{0e} at the target (blue) and the maximum upstream temperature on the given profile T_u (black), both from the B2-EIRENE fluid code. Profiles A (a) with a less significant and B (b) with a significant temperature gradient are displayed. The characteristic is normalized to the ion saturation current.

to an upstream density, more precisely the density at the midplane. For comparison, the temperatures predicted by the B2-EIRENE fluid code for the target T_{0e} and the maximum upstream temperature on the profile, T_u are also plotted. The upstream location is simply chosen as the place of maximum temperature on the given profile.

For the inner divertor target, Fig. 4.3(a), Langmuir probes should predict overestimation of T_e measurements by factors in the range from ~ 1.5 to ~ 2 for intermediate midplane densities. On the other hand, for the outer divertor target, Fig. 4.3(b) probes seem to measure correct values of T_e, except for the low density cases.

The reason why inner target probes overestimate the temperature while outer probes do not seems to be clear. The standard TCV divertor geometry is poloidally assymetric. The inner divertor leg is short which means that the distance from the target to the hot upstream

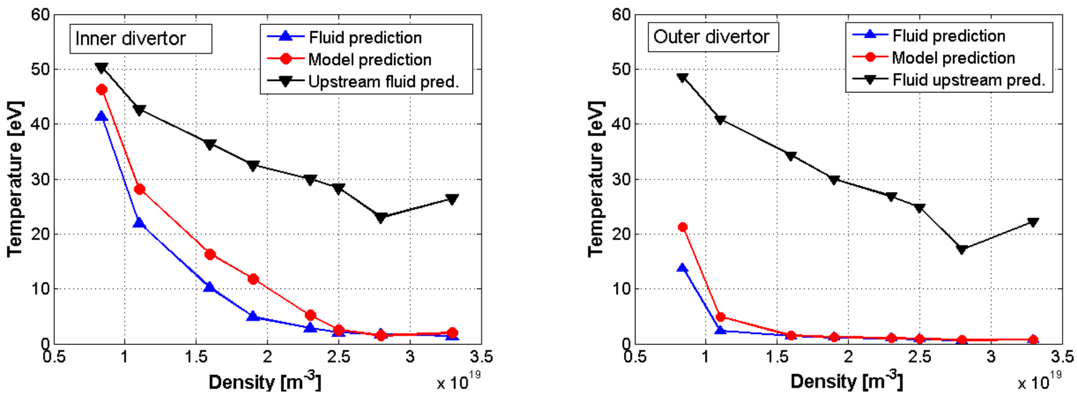

(a) (b)

Figure 4.3: Density scan of T_e predicted by the model compared to the temperature T_{0e} at the target and the maximum upstream temperature T_u, both from the B2-EIRENE generated parallel profiles.

regions is small. This gives rise significant temperature gradients. On the contrary, the outer divertor leg is long, flattening the temperature profile out, which can clearly be visible in Fig. 3.2. Electrons from the hot upstream regions have to travel a significantly greater distance to the outer target, making collisions more probable, hence distribution functions at the target are considerably less affected by these fast electrons.

4.1.3 Comparison with results in [7]

The results obtained by our model are in good accordance with the results in the paper of J. Horáček [7]. In the paper, outer divertor targets probes are expected to yield correct values of T_e, except for the low density cases, as in our model. For the inner divertor target, probes tend to overstimate the temperature for densities ranging form $10\times10^{-18}\mathrm{m}^{-3}$ to $20\times10^{-18}\mathrm{m}^{-3}$, which is in fair accordance with our predicition.

4.2 Results for JET

4.2.1 Density scan for JET

For JET input data, the same simulation has been run. The simulated temperatures measured by Langmuir probes are obtained in the same manner as for TCV. At this point, only the density scan will be shown (scanning through the density at the stagnation point), Fig. 4.4 since it sums up the most important results of the model.

It can be seen that according to the model, JET divetor target Langmuir probes should measure the temperature correctly, both for the inner 4.4(a) and outer 4.4(b) target, except for intermediate densities. The JET divertor has an approximately symmetrical divertor geometry, hence making the profiles symmetrical, Fig. 3.3 at least compared to TCV, thus giving the same result for both the inner and outer divertor target probe.

For illustration, in Fig. 4.5 the new synthetic electron energy distribution function (EVDF) at the target is plotted along with the Maxwellian EVDFs for the divertor and upstream temperatures, predicted by EDGE2D/EIRENE, for an intermediate density case, $n_{e,sep,omp} = 1.2 \times 10^{19}$ m^{-3}.

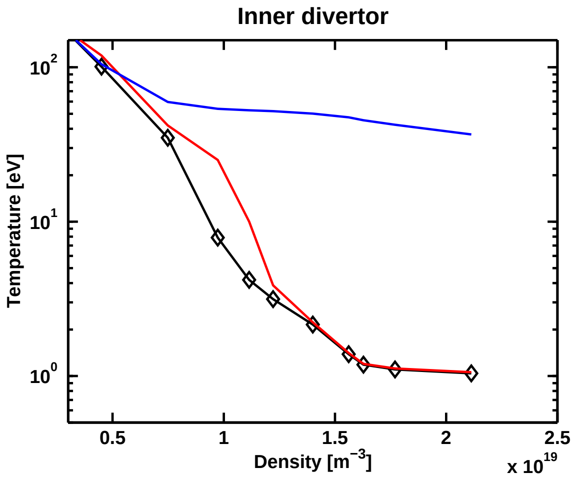

(a)

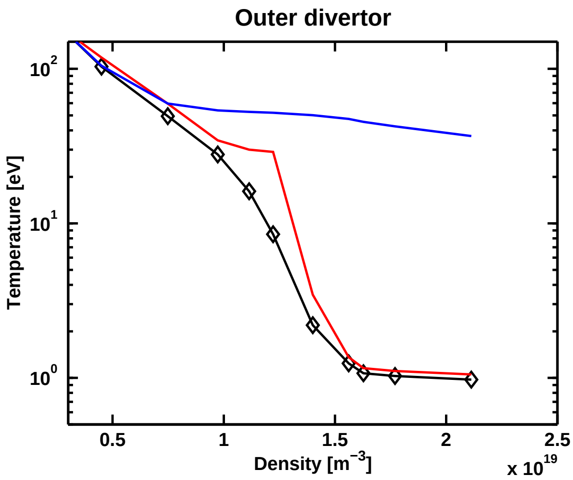

(b)

Figure 4.4: Density scan of T_e predicted by the model compared to the temperature T_{0e} at the target and the maximum upstream temperature T_u, both from the EDGE-2D generated parallel profiles.

4.2.2 Interpretation of results

The results of the simulations trigger a need to understand the connection between the shape of the parallel profiles and the result. For a low density case, no overestimation is predicted. This is not surprising, since both the density and temperature profiles are flat, Fig. 3.3, profile with the label E.

For an intermediate density case, Fig. 3.3, profile with the label F, the temperature profiles has a steep gradient coming up from both divertors. The density at the divertors is increasing as the high recycling regime is achieved. For this case, our code tends to predict temperature overestimation by divertor LPs. This is believed to be given by the fast electrons originating in the upstream high temperature regions.

For the high density case, Fig. 3.3, profile with the label G, even a steeper temperature gradient is present. We would naturally expect even more significant overestimation by LPs predicted by our model. However, our model doesn't predict overestimation. The reason for

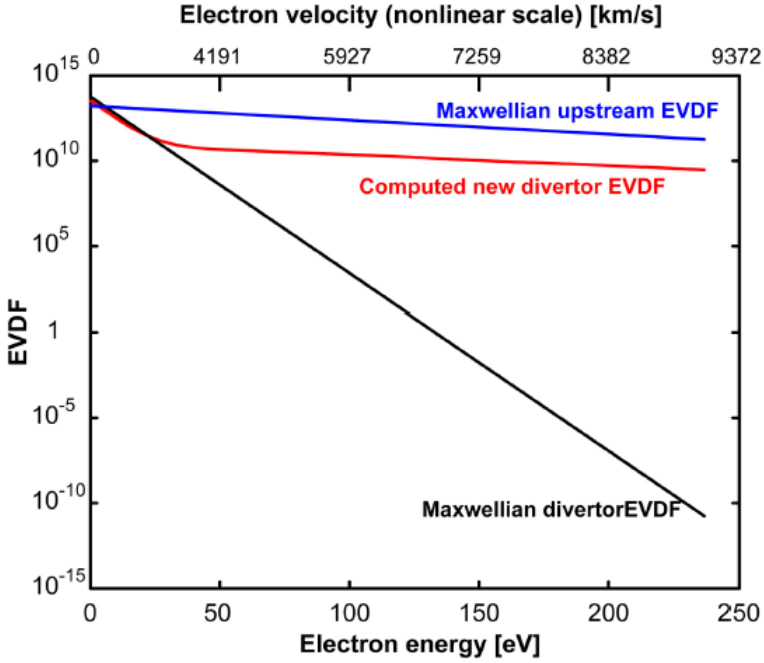

Figure 4.5: Logarithmic plots of EVDFs. On the bottom x-axis, the velocity is rescaled to energy, so that combined with the logarithmic scaling, the Maxwellian appears as a linear function. On the top x-axis is are the corresponding velocities. The synthetic EVDF at the target (red) is plotted along with the Maxwellian EVDFs for the divertor (black) and upstream (blue) temperatures, predicted by EDGE2D/EIRENE. It is visible, that the synthetic EVDF lies somewhere in between the divertor and upstream Maxwellian EVDFs

this unexpected behaviour is believed to be in the very high density in the divertor region for this case. The mean free path even for fast electrons is very low, thus the large density peaks in the divertor region can be regarded as "barriers" for the super thermal electrons originating upstream. As they cannot penetrate into the divertor region, they do not affect probes.

The of the high density barriers can be demonstrated in this synthetic experiment. This can be done by choosing a profile with high divertor densities. Next, the profile is modified by a way that the density barriers are leveled out to upstream values. This is illustrated in Fig. 4.6. The temperature profile remains unchanged, Fig. 4.7.

When we run the code for the unmodified case, no temperature overestimation by probes is predicted. However, by using the modified density profile, the code predicts that probes would measure 40 eV, while EDGE2D says the temperature at the divertor is 1 eV. This analysis confirms that the density peaks at the divertors prevent fast electrons from reaching the target.

4.2.3 Comparison with experimental LP data

Our simple model uses parallel profiles from the EDGE2D/EIRENE fluid code, which models JPNs 81469-81480. Fortunately, the JET divertor Langmuir probe diagnostic (KY4D) was in operation during the session, and validated data from the KY4D diagnostic responsible officer were provided. As explained in sections above, the main independent parameter in our analysis is the midplane separatrix density. Hence, Divertor LP data in 3 density cases,

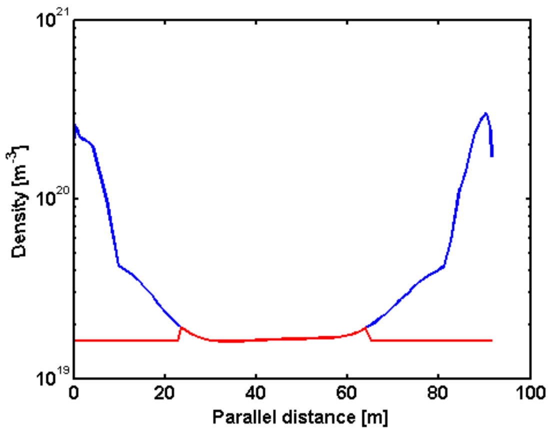

Figure 4.6: Illustration of the modified density profile. The synthetically modified profile is red while the original high density barriers are blue. In upstream locations the original and modified profiles are the same.

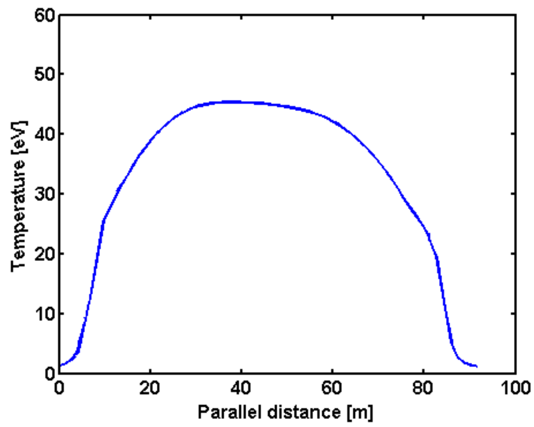

Figure 4.7: The temperature profile used in the synthetic experiment, naturally corresponding to the unmodified density profile from EDGE2D.

namely a low, intermediate and high density case were used for the comparison. The LP data are plotted in Fig. 4.8. This kind of data can be experimentally aquired by sweeping the separatrix. The peak at $dS_{\mathrm{sep}} = 0$ is the strike point and the part without data corresponds to the gap between the divertor tiles. The description of pulses from which the LP data comes from is in Tab. 4.1.

Provided the LP data, we have made a first comparison of our model results (which de facto gives a synthetic LP diagnostic) with the real experimental data. The nature of the comparison is simple. We choose a flux surface, in our case the surface situated 5 mm from the separatrix. Here we read the probe signal, and also from Tab. 4.1 we have the corresponding outer midplane separatrix density ($n_{e,\mathrm{sep,omp}}$), from HRTS. Now we have to find an EDGE/2D run that matches the midplane separatrix density of the LP data. After we find the run, we read the parallel T_e and n_e profiles on the corresponding flux surface (i. e. 5 mm from the separatrix). These profiles we use as the input into our code and compare

Density case	**JPN**	**Time into shot**	$n_{e,sep,omp}$ **(HRTS)**	$n_{e,lav}$ **(KG1V/LID4)**
Low	81472	50 s	0.8×10^{-19} m^{-3}	1.15×10^{-19} m^{-3}
Intermediate	81484	50 s	1.05×10^{-19} m^{-3}	1.77×10^{-19} m^{-3}
High	81484	53 s	1.75×10^{-19} m^{-3}	2.95×10^{-19} m^{-3}

Table 4.1: Description of the experimental LP data inculuding the pulse number, time into the pulse, outer midplane separatrix (electron) density from high resolution Thomson scattering and line averaged density from interferometry. The midplane separatrix density found experimentally is then matched to the corresponding EDGE2D output.

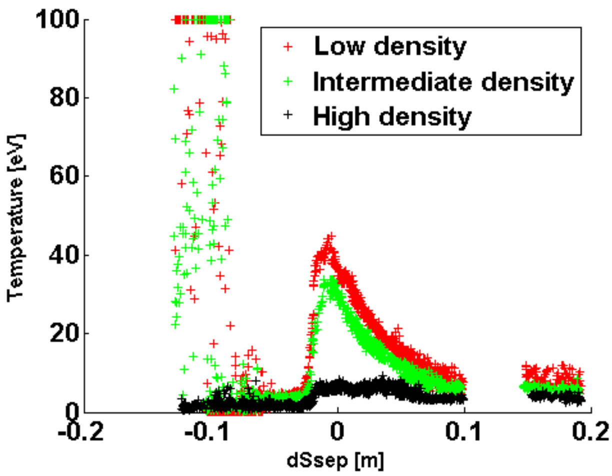

Figure 4.8: Validated experimental divertor LP data from the diagnostic RO. The plot displays the temperature at the divertor as a function of the separatrix distance, $dS_{\mathrm{sep}} = R - R_{\mathrm{sep,div}}$

.

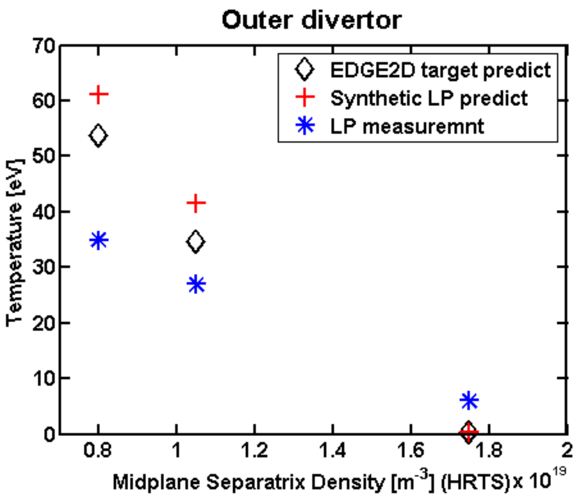

Figure 4.9: Comparison of EDGE2D/EIRENE predicted divertor temperature (diamond), synthetic temperature that the probes would hypothetically measure from our model (cross) and the experimental LP measured temperature (star).

the resulting temperature to the real experimental temperature. Such a comparison is given in Fig. 4.9

From Fig. 4.9 it is visible that for the low and moderate densities, the experimental LP temperature lies beneath the EDGE2D prediction. Our model in principle cannot yield a lower temperature than the EDGE2D prediction at the target. However, we are more interested in the high density cases, when the divertor is in the high recycling or detached regime, i. e. when the divertor temperature falls below 10 eV. Nevertheless, for the high density case, our model does not predict temperature overestimation by probes (for the reason desrcibed in section above), but the experimental probe data seem to be overestimated. This preliminary comparison suggests that the steep parallel temperature gradients are not the main cause of Langmuir probes overestimating the divertor temperature. This result is suggested also in paper [7].

A problem in our model is the reliability of the EDGE2D profiles, which is more than questionable. A way out of this may be to use profiles generated by kinetic codes, which are generally believed to be more "correct". Such data are currently available from the BIT1 kinetic code [8]. The code computes a number of quantities, including the T_e and n_e profiles. Additionally, as it is a kinetic code, the distribution functions, not necessarily maxwellian, are also calculated. In fact, whole profiles of EVDFs are available. This would pose a problem for the computation of the electron mean free path, as it could not be calculated by the simple formula anymore (the simple formula assumes maxwellian distribution). The mfp is an average quantity, thus integration over each distribution (general, non-maxwellian) should be done during each step. This would raise additional computational requirements that would possibly not be reasonable any more.

Chapter 5

Summary

The main objectives of this thesis were the improvement of the code computing the electron velocity distribution function at JET divertor targets and comparing simulation predicted Langmuir probe measurements to relevant experimental data from JET divertor LPs. In the first chapter of the thesis, a brief description of design of the JET tokamak is given, with emphasis on the constructional requirements of a device of this size, including a list of basic installed diagnostics. Next, a principles of operation of Langmuir probes is given, with characteristics of single, double and triple probes and their advantages/disadvantages.

In chapter 3, the issue of Langmuir probe T_e overestimation at divertor targets was discussed. Two possible treatments have been described, computationally demanding PIC simulations and, in contrast, a simple kinetic model. This second approach comprises of the calculation of EVDFs at the divertor targets using parallel SOL profiles of T_e and n_e generated by fluid codes. Synthetic Langmuir probe IV characteristics are then computed from the EVDFs. The value of the electron temperature is determined from these synthetic IV characteristics in the same way as from experimental Langmuir probe IV data. This part includes the improvements that have been done, namely the introduction of a variable step length computed as a fraction of the local electron mean free path. An explanation of the input data for the JET case is given, characterizing the available EDGE2D/EIRENE parallel profiles.

Lastly, in chapter 4, simulation results for both TCV and JET input data are presented. It is found that significant parallel temperature gradients distort the target EVDF, more precisely, they enhance the tail of the distribution, which afterwards leads to overestimation of Langmuir probe measurements. The main result for TCV is that for the inner divertor target, Langmuir probes should predict overestimation of T_e measurements by factors in the range from ~ 1.5 to ~ 2 for intermediate midplane densities. On the other hand, for the outer divertor target, probes seem to measure correct values of T_e, apart from the low density cases. These results are consistent with paper [7].

For the more important JET case, simulations predict the following:

1. For low densities, probes should measure correclty. Explanation: T_e and n_e gradients are not present in these cases.

2. For intermediate densities overestimation of factor up to 3 is predicted. Explanation: Large T_e gradients, n_e profile fairly flat.

3. For high densities, no overestimation predicted, i.e. probes should measure correctly. Explanation: Large T_e gradient but in contrast to intermediate densities, density peaks

are present at divertor plates (high recycling and detached regimes), acting as barriers for fast electrons originating further upstream.

The comparison with real experimental LP data is important for the high density case, since this is the case when overestimation by probes is reported. As stated above, for the high density case, according to our model, the effect of fast electrons is negligible. This suggests that the cause of overestimation may be different than fast electrons. On the other hand, the comparison performed so far is preliminary and more cases should be verified.

Finally, the use of input data from the kinetic BIT1 code is discussed. These data contain full non-maxwellian distribution functions along the whole profile, which means that the mean free path could not be calculated by a simple formula. The implementation of this would be demanding and is to be considered.

List of acronyms

ASDEX Axially Symmetric Divertor Experiment

RO Responsible officer

JET Joint European torus

EFDA European Fusion Development Agreement

ELM Edge Localized Mode

EURATOM European Atomic Energy Community

EVDF Electron Velocity Distribution Function

IR Infrared

LCFS Last Closed Flux Surface

LP Langmuir Probe

MAST Mega Amper Spherical Tokamak

PIC Parcticle in Cell

SOL Scrape-off layer

TCV Tokamak à Configuration Variable

TEXTOR Tokamak Experiment for Technology Oriented Research

Bibliography

[1] J. Wesson, *The science of JET*, IoP, 2006.

[2] *Design Proposal for the Joint European Torus - EUR-JET-R5*, European Comission, Luxembourg, 1973.

[3] P. C. Stangeby *The plasma boundary of magnetic fusion devices*, IoP, 2000.

[4] I. H. Hutchinson, *Principles of plasma diagnostics*, Cambridge University Press, 2002.

[5] K. Jesko, *Okrajové plazma v tokamacích*, Bakalářská práce, 2012

[6] M. Groth et al., *Impact of Carbon and Tungsten as Divertor Materials on the Scrape-off Layer Conditions in JET*, IAEA Proceedings, preprint, 2012

[7] J. Horáček et al., *Predicted effects of parallel temperature gradients on the overestimation of TCV divertor target Langmuir probe Te measurements*, Journal of Nuclear Materials 313-316 (2003) 931-935.

[8] D. Tskhakaya et al., *Interpretation of divertor Langmuir probe measurements during ELMs at JET*, Journal of Nuclear Materials 415 (2011) 860-864.

[9] P. C. Stangeby, *Correction to Te values measured by a Langmuir probe allowing for weak collisionality of fast electrons*, in preparation

[10] A. Pochelon et al., *Energy confinement and MHD activity in shaped TCV plasmas with localized electron cyclotron heating*, Nuclear Fusion, Vol. 39, No. 11Y (1999) 1807-1818.

[11] J. D. Swift, M. J. Schwarz, *Electric probes for plasma diagnostics*, Elsevier, London, 1969.

[12] G. F. Matthews et al., *Tokamak plasma diagnosis by electrical probes*, Plasma Phys. Control. Fusion 36 (1994) 1595.

[13] R. D. Monk et al., *Interpretation of ion flux and electron temperature profiles at the JET divertor target during high recycling and detached discharges*, Journal of Nuclear Materials 241–243 (1997) 396–401.

[14] G. Fussmann, U. Ditte, W. Eckstein, et al., *Divertor parameters and divertor operation in ASDEX*, Journal of Nuclear Materials 128-129 (1984) 350–358.

[15] J. D. Huba, *NRL plasma formulary*, Naval Research Laboratory, 2007.

[16] J. Wesson, *Effect of temperature gradient on plasma sheath*, Plasma Phys. Control. Fusion 37 (1995) 1459.

[17] D. Reiter, M. Baelmans and P. Börner, *The EIRENE and B2-EIRENE codes*, Fusion science and technology vol. 47 (2005) 172-186.